FATIGUE PROPAGATION OF INTERFACE DAMAGES IN LAYERED COMPOSITES

Pietro Ballarin[1], Daniele Fanteria[2], Maikel Khella[1], Andrea Baldi[3], Alessandro Airoldi[1]

[1] Politecnico di Milano, Department of Aerospace Science and Technology, pietro.ballarin@polimi.it
[2] University of Pisa, Civil and Industrial Engineering Department
[3] Leonardo Helicopters Division

Abstract: Composites are widely adopted to produce aeronautical structural elements because of their low weight and high strength and stiffness. Damage tolerance approach requires the analysis of damage propagation under cyclic loadings, therefore, the development of Finite Element (FE) techniques is of paramount relevance to design primary composite structures. In this work, fatigue damage accumulation laws are implemented into Cohesive Zone Models (CZM) and validated on pre-damaged L-shaped Carbon Fiber Reinforced Polymer (CFRP) specimens subjected to cyclic loading in a tensile test machine. Static and fatigue tests were performed on the specimens, and results shown that the number of cycles corresponding to the load drop seems to be captured with a satisfactory accuracy. The value of the load reached after the drop seems to be slightly overestimated by the FE model, this behaviour could be explained considering the high sensitivity to the mesh size of the fatigue damage model and the crack migration phenomenon occurring in the curved region.

Keywords: cohesive zone model; fatigue; composites; carbon fiber; delamination

INTRODUCTION

Composite materials exhibit excellent properties, such as high stiffness and strength combined with low density, making them well-suited for aerospace structural applications. However, despite their high performance along the fibre direction, their properties in the transverse direction remain a critical concern. Specifically, delamination is one of the most common and dangerous failure modes in composite laminates [1]. This type of damage can grow under applied loads while remaining undetected and may originate either during manufacturing or during the service life of the structure, as a result of load exceedance or low-velocity impacts [2]. Internal damages can grow not only as a consequence of the load exceedance, but even at lower magnitudes loads repeated cyclically: this phenomenon is known as fatigue, and it represents a critical issue for structural integrity. Indeed, fatigue as it is a leading cause of failure and enables damage or defects to propagate even under stress levels below the static strength [3]. Over the years, various Finite Element (FE) approaches based on the Cohesive Zone Model (CZM) have been developed to predict the interlaminar residual static strength of composite structures [4, 5]. However, the relevance of the fatigue phenomenon in the structural design, led some authors more recently to develop new methods to simulate damage propagation under fatigue loading conditions [6–

11]. Since simulating each fatigue cycle would result in unacceptable computational times, most of these approaches employ the Simplified Cyclic Loading (SCL) principle. This method involves applying a constant static load or displacement corresponding to the maximum load in the fatigue cycle. The fatigue cycles are then simulated over a fictitious time period during which the toughness of the interface elements is gradually degraded.

Most existing numerical approaches have been validated using standard specimens and testing procedures, such as Double Cantilever Beam (DCB) for mode I delamination or End Notched Flexure (ENF) for mode II delamination: this study seeks to validate a numerical model for fatigue damage accumulation in a more complex and representative structural sub-component—specifically, an L-shaped geometry.

This paper is organized as follows: (i) in the Methods section, fatigue damage laws presented in literature are implemented in the CZM and calibrated using Mode I experimental crack propagation data from the literature. The FE models of the DCB and L-shaped specimens are presented, along with details of their manufacturing and testing processes; (ii) in the Results section, the correlation of the fatigue damage laws in simple DCB specimens are presented along with the experimental results of static and fatigue tests on pre-cracked L-shaped specimens. Then, the numerical results obtained with the fatigue damage law previously calibrated on DCB specimens are shown; (iii) in the Conclusions section, the main findings are summarized, and directions for future research are proposed.

METHODS

This section is organized in three subsections: (i) in the first subsection, an existing fatigue damage law is presented and the FE model of the DCB used for the calibration of the model is described; (ii) in the second subsection, the manufacturing process and test setup of the L-shaped specimens is presented; (iii) in the last subsection, the FE model of the L-shaped specimen adopted to validate the fatigue damage law is described.

Calibration of fatigue damage law in mode I

A FE model of a DCB specimen was created using Simulia/Abaqus Explicit, the thickness of the specimen was set to 4.5 mm, and the width was set equal to 2 mm as only a stripe of the specimen was considered. The out-of-plane displacements were constrained on one side of the specimen. The FE model of the specimen is presented in Figure 1a.

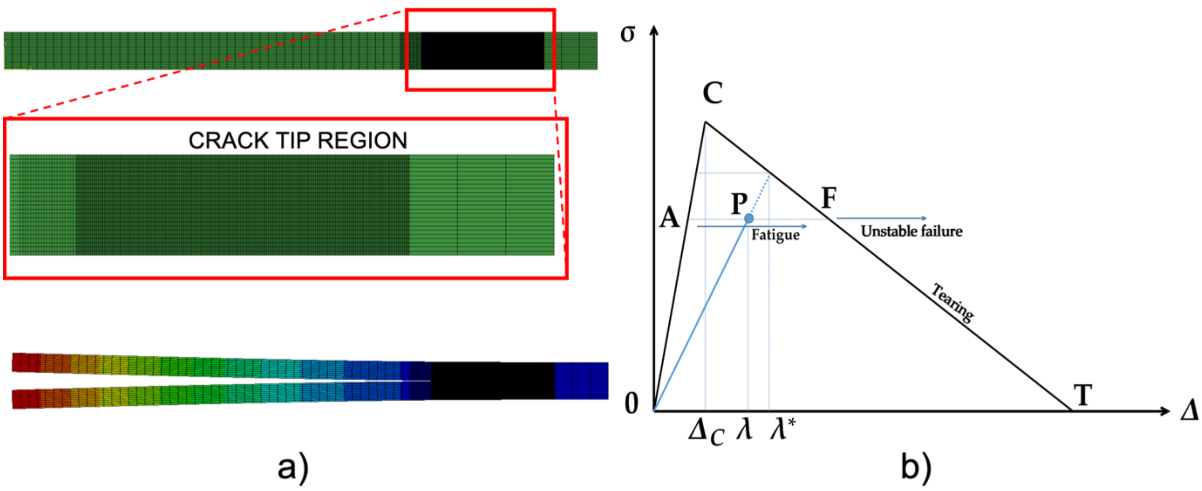

Figure 1: a) Finite Element model of the DCB specimen; b) cohesive law with fatigue damage.

The arms were modelled with continuum shell elements SC8R, and a layer of cohesive elements COH3D8 having a thickness of 0.01 mm was adopted to model the interface between the two arms, the penalty stiffness was set according to [12] and the parameter α was set equal to 50. The length of the pre-crack was fixed at 50 mm, and the elements size was set equal to 0.1 mm in the crack tip region along the crack propagation direction, while a coarser mesh was adopted far from the crack. A total of

12 elements were used mesh each arm along the thickness direction. The properties of the material are presented in Table 1, normalized with respect to the stiffness along the fibre direction E_{11} for confidentiality reasons.

Table 1: Normalized material properties.

Name	*Normalized value*
E_{11}	1
E_{22}	0.059
G_{12}	0.035
ν_{12}	ν_{12}

The fatigue damage accumulation law presented in [9], and based on the SCL approach, was implemented in cohesive elements. The following damage accumulation law presented in Eqn. 1 was therefore implemented.

$$\frac{dD}{dN} = \frac{1}{\gamma} \frac{(1-D)^{-q}}{E^{\beta}(\beta+q+1)} \left(\frac{\lambda}{\lambda^*}\right)^{\beta} \tag{1}$$

Where N represents the number of fatigue cycles, γ represents the number of cycles to endurance, E represents the relative endurance limit, β represents the exponent of the S-N curve, and it can be calculated according to Eqn. 2.

$$\beta = \frac{-7\eta}{\log(E)} \tag{2}$$

Where the variable η represents the brittleness parameter. The parameter q presented in Eqn. 1 represents a model parameter, while the variables λ and λ^* represent the separation displacement of the cohesive element, and they can be observed in Figure 1b. The variable D, the damage norm, is calculated according to Eqn. 3.

$$D = \frac{\lambda^* - \Delta_C}{\Delta_F - \Delta_C} \tag{3}$$

Where Δ_F and Δ_c represent the displacement jump to failure of the cohesive and the displacement jump for the onset of the damage, respectively.

Test setup and specimens' preparation procedure

The L-shaped specimens were produced using the unidirectional Carbon Fibre Reinforced Polymer (CFRP) AS4/8552, having a ply cured thickness of 0.13 mm. A total of 48 plies having the same orientation along the curved shape of the specimen were stacked on a mould having a curvature radius of 6.4 mm, which can be seen in Figure 2a. Between the 16th and the 17th ply, corresponding to the 1/3 of the lamination sequence, a 2 mm width non-adhesive Teflon layer was inserted to form the pre-crack. The vacuum bag was closed on the mould and the laminate was then put in autoclave and cured according to the Manufacturer Recommended Curing Cycle (MRCC) at 180°C at a pressure of 7 bar.

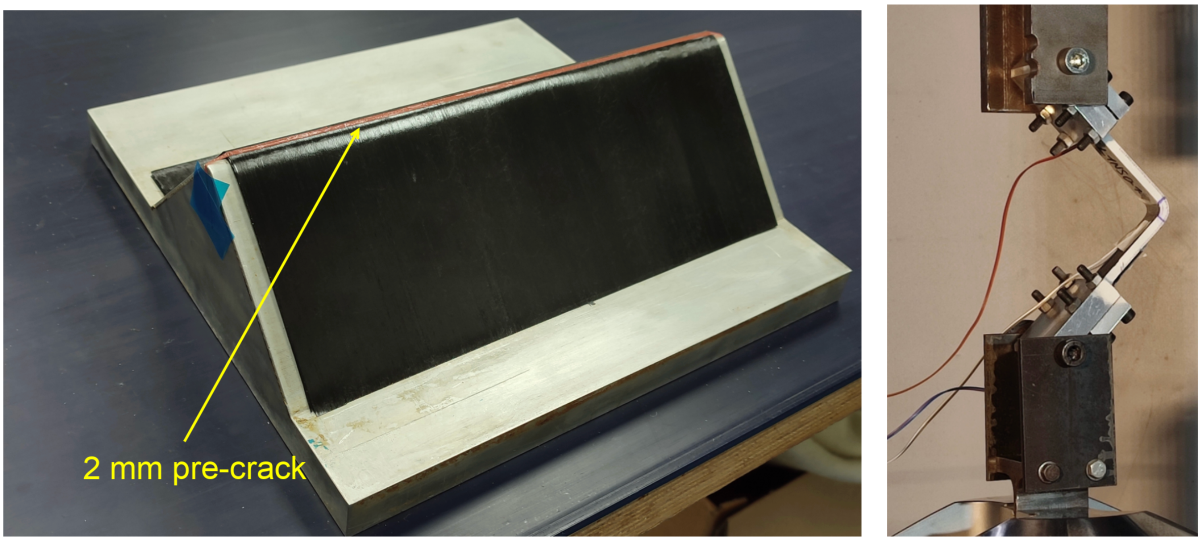

a) b)

Figure 2: a) lamination of L-shaped specimens with detail of the pre-crack; b) test setup of L-shaped specimens.

The specimens were then cut from the panel with a saw obtaining a width of 20 mm, a thickness of 6.28 mm, and a leg length of 88 mm. Each specimens' end was then clamped for a length of 30 mm in a fork, as it can be seen in Figure 2b, and the edge was covered with a which powder to visualize the crack. The edge of the specimen was then marked to measure the crack length.
The test was conducted on a MTS 810 Mini Bionix tensile test machine in displacement control, and with a displacement ratio R equal to 0.1 at a frequency of 6 Hz.

Finite Element model of L-shaped specimen

The FE model of the L-shaped specimen is presented in Figure 3. In Figure 3a the entire specimen's model can be seen. The displacement was imposed through some reference points, positioned in correspondence of the pin's axis visible in Figure 2b, connected rigidly to the first 30 mm of the specimen's legs, corresponding to the region where the specimen was clamped in the experiment.

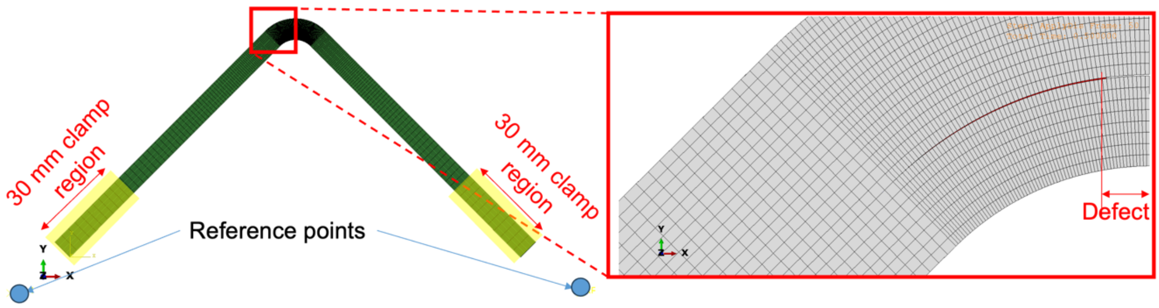

a) b)

Figure 2: a) Finite Element model of the L-shaped specimen; b) detail of the meshing technique in the pre-damaged central region.

In Figure 3b, the detail of the meshing strategy can be observed. A layer of 0.01 mm thick cohesive elements COH3D8 was interposed in the interface where the pre-damage was positioned, at 1/3 of the lamination sequence from the internal surface. The penalty stiffness of the cohesive was kept the same as of the DCB model previously presented. The other regions of the specimen were meshed using continuum shell elements SC8R type. The width of the model was 2 mm, corresponding to 1/10 of the width of the entire specimen, the out-of-plane displacements were constrained on one face of the model, indeed, preliminary assessments highlighted the stiffening effect obtained imposing the constraint to both the specimen's faces. A total of 24 elements were distributed along the thickness direction, while in the curved region of the specimen the elements had a characteristic length equal to 0.1 mm, a coarser mesh instead was adopted outside that region. The 2 mm defect, visible in Figure 3b, was obtained eliminating the cohesive elements in correspondence of the region where the non-adhesive insert was positioned.

RESULTS

Fatigue damage law calibration

Different values of displacement were imposed to the DCB model presented in the previous section, specifically, the values of 1.48 mm, 1.70 mm, 1.92 mm, and 2.25 mm were imposed. The results can be observed in Figure 4, where the experimental data were fitted with the results obtained with the FE.

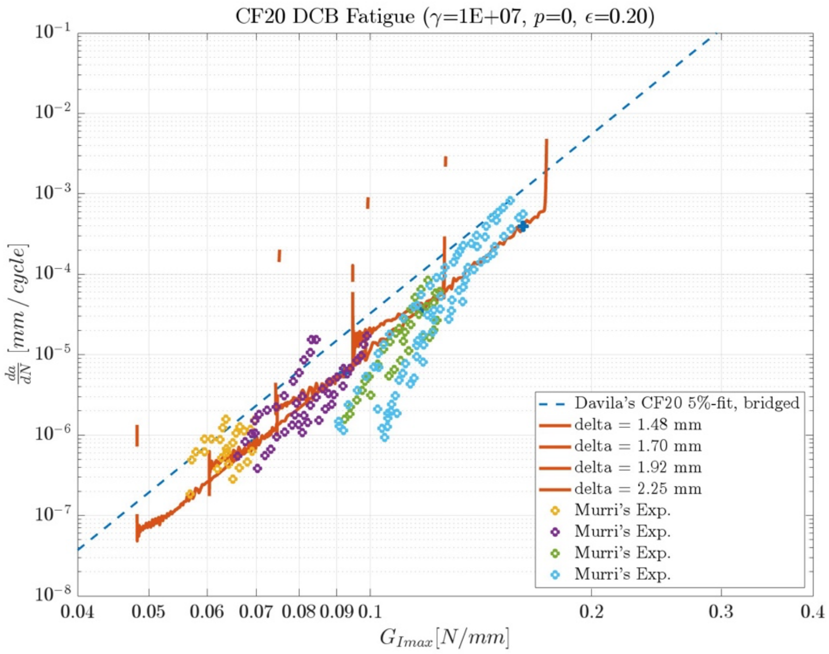

Figure 4: experimental data of IM7/8552 obtained by [13] and results obtained with FE in mode I for stress ratio R = 0.1.

The same parameters of the damage law CF20 presented in [9] were used, and they are hereby reported in Table 2 for completeness.

Table 2: parameters of the fatigue damage accumulation law CF20.

Name	*Value*
η	0.95
ε	0.2
p	0
γ	10^7

Overall, results seem to have a good fit with the experiments especially for the results obtained at lower initial severity.

Validation on L-shaped specimen

First, a static test on two specimens was carried out to set a proper value of initial severity, the test results in terms of normalized force vs normalized displacement are presented in Figure 5a.

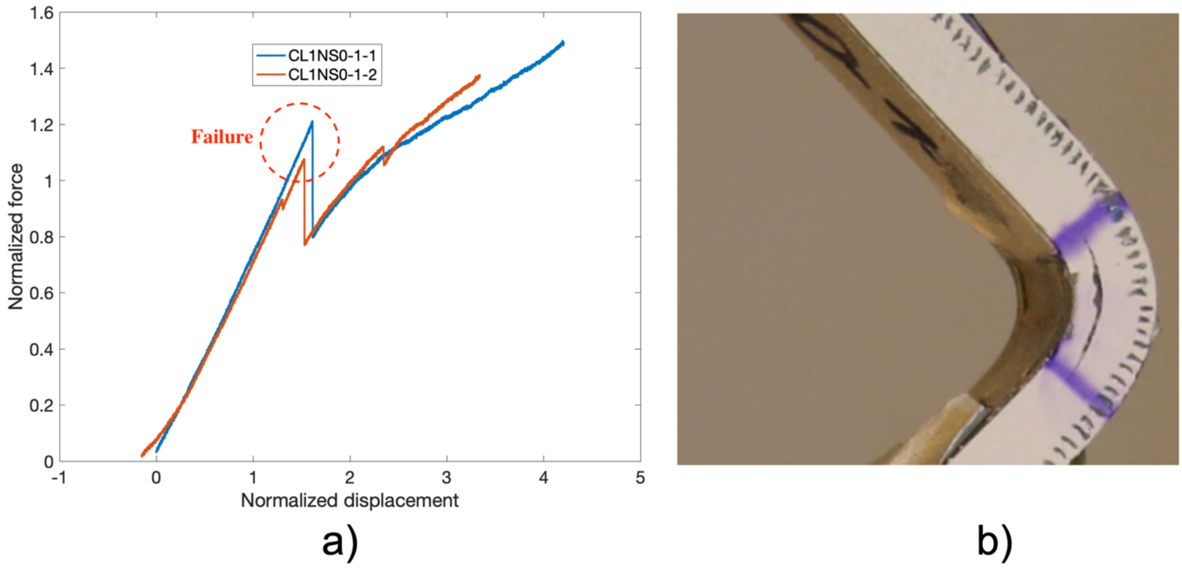

Figure 5: a) static test on two specimens CL1NS0-1-1 and CL1NS0-1-2. Force and displacements are normalized for confidentiality reasons.

As it can be seen the specimens failed approximately at normalized load equal to 1.1 and normalized displacement equal to 1.5 in correspondence of the pre-cracked interface, the failure is visible in Figure 5b.

The fatigue damage model CF20 was validated on the L-shaped specimens subjected to fatigue cycles. The same models parameters providing the results presented in Figure 4 were adopted. The experiments were conducted imposing different values of initial severity, defined as in Eqn. 4 by the squared ratio between the maximum displacement during the fatigue cycle and the displacement to failure.

$$Severity = \left(\frac{\delta_{\max fatigue}}{\delta_{failure}}\right)^2 \tag{4}$$

In Figure 6, the comparison between experimental and numerical force vs number of cycles are presented for different values of initial severity: 0.59, 0.32, and 0.27, corresponding to Figure 6a, Figure 6b, and Figure 6c, respectively.

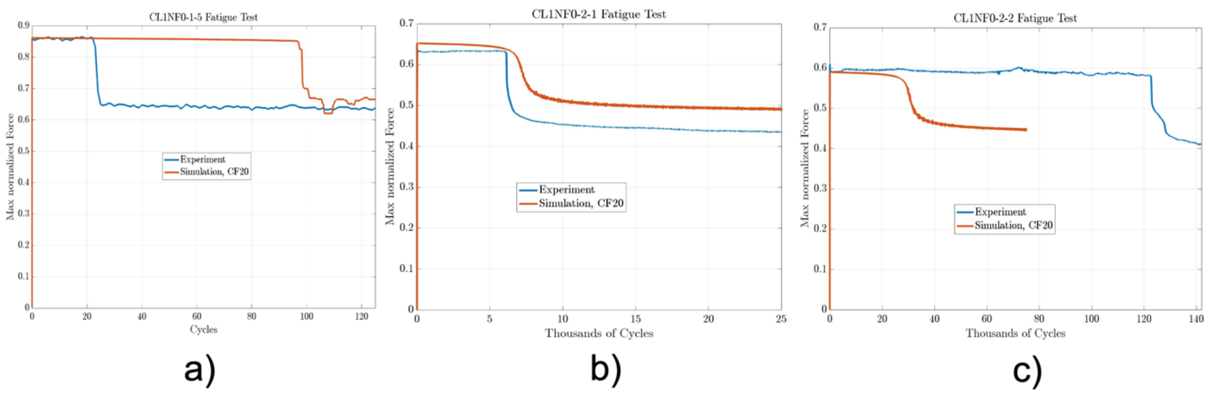

Figure 6: numerical-experimental results comparison of maximum normalized force vs number of fatigue cycles for initial severity of a) 0.59; b) 0.32; c) 0.27.

In all the cases presented in Figure 6 a load drop is observed at a certain number of cycles: this corresponds to an acceleration of the crack propagation rate since the Energy Release Rate (ERR) is not monotonically decreasing as the crack advances, on the contrary, the ERR increases for small crack lengths reaching a maximum value after which a monotonic decreasing behaviour is achieved.

It can be observed in Figure 6a that for an initial severity equal to 0.59, the load drop is estimated by the FE model to be around 100 cycles, while the experiment shows a load drop at about 20 cycles. The load drop seems to be well captured in Figure 6b, where the latter occurs at about 6000 fatigue cycles for the experiment and the FE model, while the result presented in Figure 6c, the one at the lower initial severity, shows the FE model estimating a load drop at about 30000 fatigue cycles, while the experimental load drop occurs at about 120000 fatigue cycles.

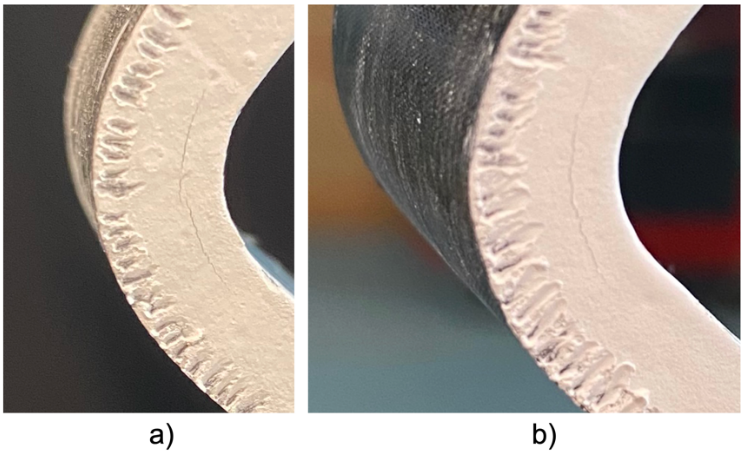

Figure 7: a) final failure of the specimen tested at initial severity 0.32; b) final failure of the specimen tested at initial severity 0.27.

After the occurrence of the load drop, the crack reached the end of the curved region of the specimen, as it can be observed in Figure 7, however, it can be seen that in Figure 7a a crack migration occurred, and a delamination was observed in an interface different from the one where the pre-crack was positioned. Another consideration is worth to be made about the load level reached after the drop, indeed, while in the first case (Figure 6a) a similar load is reached for the simulation and the experiment, in the other cases the load seems to be slightly overestimated, particularly in Figure 6b, the reason could be the change of the mesh size in correspondence of the end of the curved part of the specimen. Indeed, as presented by other authors, such type of fatigue models exhibit a high sensitivity to the mesh size, therefore, once the crack reaches the end of the curved region, visible in Figure 2b, the further propagation of the crack could be prevented.
Overall, considering the high scatter typical of the fatigue, especially for low values of severity, and considering the crack migration observed during the test, which could not be captured by the FE model, the fatigue model seems to provide satisfactory results even in more complex and representative aeronautical structural elements.

CONCLUSIONS

This study demonstrated the feasibility and accuracy of a fatigue damage model based on the CZM for simulating delamination growth in composite structures under cyclic loading. The model was first calibrated using Mode I DCB specimens and then validated on more complex L-shaped composite specimens, representative of aeronautical components.
The numerical results showed good agreement with experimental data in terms of the number of cycles to significant crack propagation. While some discrepancies were noted at low severities, likely due to mesh sensitivity and unmodeled crack migration phenomena, the overall correlation supports the model's effectiveness.
This work extends the application of fatigue CZM modeling beyond standard specimens to structurally representative geometries, indicating its potential for integration into future aerospace structural design and certification processes. Future works should focus on enhancing the model's robustness against mesh sensitivity, and validating against a larger number of tests to mitigate the effects of the statistics variability.

REFERENCES

[1] Wisnom, M. R. (2012), *Philos. Trans. R. Soc. A*, vol. 370, n. 1965, p. 1850.
[2] Reid, S. R., Zhou, G. (2000), *Impact behaviour of fibre-reinforced composite materials and structures*, Elsevier, Boca Raton FL, USA.
[3] Vassilopoulos, A. P., Keller, T. (2011), *Fatigue of fiber-reinforced composites*, Springer Science & Business Media.
[4] Airoldi, A., Sala, G., Bettini, P., & Baldi, A. (2013), *J. Reinf. Plast. Compos.*, vol. 32, n. 15, p. 1075.
[5] Turon, A., Camanho, P. P., Costa, J., Renart, J. (2010), *Compos. Struct.*, vol. 92, n. 8, p. 1857.
[6] Turon, A., Costa, J., Camanho, P. P., Dávila, C. G. (2007), *Compos. -A: Appl. Sci. Manuf.*, vol. 38, n. 11, p. 2270.
[7] Teimouri, F., Heidari-Rarani, M., Aboutalebi, F. H. (2021), *Comp. Struct.*, vol. 263, n. 113716.
[8] Pakravan, A., Taheri-Behrooz, F. (2024), *Compos. -A: Appl. Sci. Manuf*, vol. 181, n. 108112.
[9] Dávila, C. G., Rose, C. A., Murri, G. B., Jackson, W. C., & Johnston, W. M. (2020). *Evaluation of fatigue damage accumulation functions for delamination initiation and propagation* (No. NF1676L-36100).
[10] Allegri, G. (2020), *J. Mech. Phys. Solids*, vol. 138, n. 103900.
[11] Leone, F. A., Davila, C. G. (2021). In: Proceeding of the AIAA Scitech 2021 Forum, p. 0314.
[12] Turon, A., Davila, C. G., Camanho, P. P., Costa, J. (2007), *Eng. Fract. Mech.*, vol. 74, n. 10, p. 1665.
[13] Murri, G. B. (2013). *Evaluation of delamination onset and growth characterization methods under mode I fatigue loading* (No. NASA/TM-2013-217966).